

1 **Application of airborne LiDAR data and**
2 **airborne multispectral imagery to structural**
3 **mapping of the upper section of the Troodos**
4 **ophiolite, Cyprus**

5 Stephen Grebby^{a,*}, Dickson Cunningham^a, Jonathan Naden^b, Kevin Tansey^c

6 ^a*Department of Geology, University of Leicester, University Road, Leicester LE1*
7 ^a*7RH, UK*

8 ^b*British Geological Survey, Keyworth, Nottingham NG12 5GG, UK*

9 ^c*Department of Geography, University of Leicester, University Road, Leicester*
10 ^c*LE1 7RH, UK*

11

12 *Corresponding author. Tel: +44 (0)116 252 3922

13 Fax: +44 (0)116 252 3918

14 Email address: srg11@le.ac.uk

15

16 **Abstract** Structural maps are traditionally produced by mapping features such as faults,
17 folds, fabrics, fractures and joints in the field. However, large map areas and the spatially limited
18 ground perspective of the field geologist leads to the inevitability that some important geological
19 features may go un-noticed. The ability to recognise and map both local and regional structural
20 features using high-resolution remote sensing data provides an opportunity to complement field-
21 based mapping to enable the generation of more comprehensive structural maps. Nonetheless,
22 vegetation cover can adversely affect the extraction of structural information from remotely sensed
23 data as it can mask the appearance of subtle spectral and geomorphological features that
24 correspond to geological structures. This study investigates the utility of airborne Light Detection

25 And Ranging (LiDAR) data and airborne multispectral imagery for detailed structural mapping in
26 vegetated ophiolitic rocks and sedimentary cover of a section of the northern Troodos ophiolite,
27 Cyprus. Visual enhancement techniques were applied to a 4 m airborne LiDAR digital terrain
28 model and 4 m airborne multispectral imagery to assist the generation of structural lineament
29 maps. Despite widespread vegetation cover, dykes and faults were recognisable as lineaments in
30 both datasets and the predominant strike trends of lineaments in all resulting maps were found to
31 be in agreement with field-based structural data. Interestingly, prior to fieldwork, most lineaments
32 were assumed to be faults, but were ground verified as dykes instead, emphasising the importance
33 of ground truthing. The dyke and fault trends documented in this study define a pervasive
34 structural fabric in the upper Troodos ophiolite that reflects the original sea-floor spreading history
35 in the Larnaca graben. This structural fabric has not previously been observed in such detail and is
36 likely to be continuous in adjacent regions under sedimentary cover. This information may be
37 useful to future exploration efforts in the region focused on identification of structurally controlled
38 mineral and groundwater resources. Overall, our case study highlights the efficacy of airborne
39 LiDAR data and airborne multispectral imagery for extracting detailed and accurate structural
40 information in hard-rock terrain to help complement field-based mapping.

41

42 *Keywords: Troodos ophiolite; airborne LiDAR; multispectral imagery; structural*
43 *mapping*

44

45

46

47

48

49

50

51

52

53 **Introduction**

54 In regions that have been deformed, documenting the structural geology is
55 a key objective of geological mapping (Barnes and Lisle 2004). Geological maps
56 portraying structural features are important because they provide valuable
57 information for understanding the local crustal architecture and deformation
58 history. In addition, structural maps may inform seismic and landslide hazard
59 assessments, and provide useful information for major engineering projects and
60 the exploration of groundwater, petroleum and mineral resources (Moore and
61 Waltz 1983; Kresic 1995; Karnieli et al. 1996; Wladis 1999; Harris et al. 2001;
62 Peña and Abdelsalam 2006; Corgne et al. 2010).

63 Traditionally, structural maps are produced by mapping features such as
64 faults, folds, fabrics, fractures and joints in the field. Although arguably the most
65 reliable and accurate maps are those produced using this approach, large map
66 areas, time constraints and the limited ground perspective of the field geologist
67 has the potential to increase the possibility that not all structural features will be
68 identified (Süzen and Toprak 1998). However, the ability to also recognise and
69 map structural features using remote sensing data offers the potential to provide
70 complementary information and the opportunity to generate more comprehensive
71 and accurate structural maps.

72 Many important structural features (e.g., faults, fractures, veins, dykes,
73 joints) may be expressed as lineaments in remotely sensed imagery and digital
74 elevation models (DEMs; Masoud and Koike 2006). This is particularly the case
75 with steep structures because their surface traces are less deflected and curved
76 across uneven topography. A lineament is defined by O'Leary et al. (1976) as "a
77 mappable, simple or composite linear feature of a surface, whose parts are aligned

78 in a rectilinear or slightly curvilinear relationship and which differs distinctly
79 from the patterns of adjacent features and presumably reflects a subsurface
80 phenomenon". In spectral imagery, lineaments are typically recognised as edges
81 defined by a series of adjacent pixels at the boundary of brightness changes
82 (Koike et al. 1998). Such spectral features may correspond to variations in surface
83 composition or shadowing. In the context of the topographic domain, geological
84 lineaments are typically associated with geomorphological features such as linear
85 valleys, ridgelines, escarpments and slope breaks (Jordan and Schott 2005). Such
86 features are also expressed as edges in DEMs, defined either by an abrupt change
87 in elevation (i.e., slope break) or by an increase or decrease in elevation for a short
88 lateral distance (i.e., ridgelines and valleys).

89 Lineaments observed in remotely sensed data products that are interpreted
90 to be geological structures are typically manually traced. However, this technique
91 can be time-consuming and tedious at regional mapping scales, and also highly
92 subjective and therefore irreproducible (Masoud and Koike 2006). A variety of
93 enhancement techniques are commonly used to try to improve the efficiency and
94 objectivity of the visual interpretation and mapping process. Principal Component
95 Analysis, decorrelation stretching and generation of false-colour composite
96 images are useful techniques for exaggerating subtle colour or brightness
97 differences in spectral imagery to accentuate the appearance of potential
98 lineaments (Qari 1991; Mountrakis et al. 1998). Shaded relief models generated
99 from DEMs are a powerful tool for enhancing the appearance of lineaments in
100 topographic data. This is because the artificial solar illumination azimuth and
101 inclination angles can be varied to help identify lineaments in a range of
102 orientations by recognising the shadowing effects (manifest as boundaries
103 between light and dark tones) caused by abrupt changes in elevation (Jordan and

104 Schott 2005). Additional techniques that are commonly applied to spectral
105 imagery and DEMs in order to enhance the visual appearance of edges include
106 convolution filters, such as Sobel, Prewitt and Laplacian filters (Moore and Waltz
107 1983; Süzen and Toprak 1998; Wladis 1999), and morphological operators, such
108 as erosion, dilation, opening and closing (Tripathi et al. 2000; Ricchetti and
109 Palombella 2005).

110 Automated algorithms for mapping geological lineaments from remotely
111 sensed data have also received considerable attention (Argialas and Mavrantza
112 2004). Examples include algorithms based on Canny edge detection (Corgne et al.
113 2010), the Hough transform (Karnieli et al. 1996; Fitton and Cox 1998), line-
114 tracing (Koike et al. 1995) and morphometric feature parameterisation (Wallace et
115 al. 2006). Despite increasing the reproducibility, efficiency and objectivity of
116 lineament mapping, there are concerns regarding the suitability of automated
117 algorithms for geological lineament detection (Parsons and Yearley 1986) — the
118 most obvious being their inability to differentiate geological lineaments from non-
119 geological lineaments (e.g., roads, field boundaries). Therefore, for reasonably
120 sized areas, the task of lineament mapping is arguably best performed manually
121 based on human perception.

122 Vegetation cover can have somewhat adverse effects on the extraction of
123 structural information from remotely sensed data because vegetation, especially
124 tall dense vegetation (e.g., forests), is capable of masking the appearance of subtle
125 spectral and geomorphological lineaments that correspond to geological
126 structures. Also, with only moderate spatial resolution (~ 15–30 m), the utility of
127 data acquired from classic spaceborne instruments — such as Landsat TM and the
128 Shuttle Radar Topographic Mission (SRTM) — is generally confined to the
129 identification of only regional structural features. The use of high-resolution (ca.

130 1–4 m) airborne Light Detection And Ranging (LiDAR) data and airborne
131 spectral imagery can enhance the utility of remote sensing for structural mapping
132 because these datasets enable the extraction of detailed information about both
133 local and regional geological structures. Furthermore, with the capability to
134 acquire accurate and high-resolution topographic data even in forested terrain
135 (Kraus and Pfeifer 1998), airborne LiDAR is now established as an important tool
136 for mapping the surface traces of regionally-significant faults in either vegetated
137 or non-vegetated terrain (e.g., Harding and Berghoff 2000; Haugerud et al. 2003;
138 Prentice et al. 2003; Cunningham et al. 2006; Arrowsmith and Zielke 2009).
139 Nevertheless, with the exception of a few studies which examine the use of
140 airborne LiDAR for identifying bedrock structures (Wallace et al. 2006; Nyborg
141 et al. 2007; Pavlis and Bruhn 2011), the broader utility of airborne LiDAR for
142 structural applications has yet to be fully realised.

143 The objective of this study is to investigate the utility of airborne LiDAR
144 data and airborne multispectral imagery for detailed structural mapping of the
145 vegetated ophiolitic rocks and sedimentary cover in a section of the upper
146 Troodos ophiolite, Cyprus. Owing primarily to the reliability concerns associated
147 with automated algorithms, the efficacy of airborne LiDAR data and airborne
148 multispectral imagery for structural mapping is evaluated here by manually
149 generating lineament maps with the aid of several visual enhancement techniques.
150 Structural information extracted from the data is subsequently validated using
151 field-based data.

152

153 **Geological setting**

154 The Troodos ophiolite is an uplifted slice of oceanic crust and lithospheric
155 mantle that was created through sea-floor spreading (Gass 1968; Moores and Vine
156 1971). The ophiolite forms a dome-like structure centred on Mt. Olympus
157 (1,952 m) that dominates the geology and topography of the island of Cyprus.
158 Stratigraphically, the ophiolite comprises a mantle sequence of harzburgites,
159 dunites and a serpentinite diapir, a largely gabbroic plutonic complex, a sheeted
160 dyke complex, a lava sequence and oceanic sediments at decreasing elevations
161 along the northern slopes of the range (Varga and Moores 1985). The study area is
162 situated on the contact between the lava sequence and overlying sedimentary
163 cover sequences in the northern foothills of the Troodos ophiolite (Fig. 1a). It
164 covers approximately 16 km² and contains four main lithological units — the
165 Basal Group (generally comprising 80–90% dykes and 10–20% lavas), Pillow
166 Lavas (Upper and Lower), late Cretaceous to early Miocene chalky marls of the
167 Lefkara Formation and alluvium–colluvium. This area is located in the most
168 eastern of three structural grabens (the Larnaca graben) proposed and interpreted
169 by Varga and Moores (1985) as fossil axial valleys of an eastward migrating
170 spreading centre in the northern part of the ophiolite. Faulting within this area is
171 dominated by a NW–SE trend, which is parallel to the interpreted spreading axis
172 of the Larnaca graben and is therefore consistent with the proposed crustal
173 extension in this region. Moreover, the dominant dyke trend in the study area is
174 parallel to this NW–SE faulting trend (Gass 1960). A less significant N–S
175 structural trend observed in this region is believed to correspond to a later stage of
176 normal faulting (Gass 1960; Boyle and Robertson 1984).

177 Ubiquitous vegetation typically covering between 30–90% of the surface
178 area is responsible for a lack of completely exposed outcrops in the study area.
179 Vegetation cover type generally varies from moderate-to-dense lichen cover, to
180 crops (e.g., cereals, olive groves) as well as both green and dry grasses, to what
181 can be broadly described as garrigue or maquis, predominantly comprising
182 scrubby short dry grasses, short-to-medium height shrubs and scattered small
183 trees. Other types of mostly sporadic vegetation cover occurring throughout the
184 study area include trees — ranging from isolated trees (e.g., pines and oaks) to
185 dense thickets and copses — and areas covered by tall, dry grasses and scrubland.
186

187 **Remote sensing data**

188 Airborne LiDAR data and Airborne Thematic Mapper (ATM)
189 multispectral imagery were acquired over the Troodos study area in May 2005 by
190 the Natural Environment Research Council Airborne Research and Survey
191 Facility. The airborne LiDAR data were acquired at an average flying altitude of
192 2550 m using an ALTM-3033 system operating with a laser pulse repetition rate
193 of 33 kHz and a half-scan angle of $\pm 19.4^\circ$ either side of the nadir. The resulting
194 dataset contains point data from five overlapping flight-lines, each with a swath
195 width of 1400–1500 m and an overlap of 20%–50% between adjacent swaths.
196 After initial pre-processing by the Unit for Landscape Modelling at the University
197 of Cambridge, UK, the airborne LiDAR point data were delivered as ASCII files
198 containing the x-y-z coordinates of all first and last returns in the WGS84
199 Universal Transverse Mercator (UTM) zone 36-North coordinate system. On
200 delivery, the point data were classified as either ground or non-ground returns
201 (e.g., trees, buildings) using the triangulated irregular network densification

202 algorithm (Axelsson 2000) implemented in the TerraScan software (Terrasolid
203 Ltd., Finland). Points corresponding to non-ground returns were subsequently
204 discarded, whilst those classified as ground returns were interpolated using a
205 block kriging algorithm in order to generate a 4 m digital terrain model (DTM) or
206 “bare-earth” DEM (Fig. 1b). A more detailed description of the airborne LiDAR
207 data processing steps is provided by Grebby et al. (2010).

208 The ATM imagery initially comprised 11 spectral bands located in the
209 visible/near-infrared (VNIR; Bands 1–8), short-wave infrared (SWIR; Bands 9–
210 10) and thermal infrared (TIR; Band 11) regions of the electromagnetic spectrum.
211 However, due to data quality concerns, and for the purpose of concentrating solely
212 on reflectance data, ATM Bands 1 and 11 were omitted from any further analysis.
213 Five northwest-southeast trending flight-lines of imagery were acquired over the
214 study area and delivered as Level 1b Hierarchical Data Format (HDF) files, with
215 radiometric calibration algorithms applied and aircraft navigation information
216 appended. The radiometric calibration involves conversion of the raw ATM data
217 to at-sensor radiance units, followed by scaling to 16-bit digital numbers (DNs).
218 Conversion of the raw ATM data to at-sensor radiance is achieved by applying
219 gains and offsets — determining using a source traceable to a national standard —
220 to the data recorded in each of the wavebands (Hill et al. 2010). All image strips
221 were individually geocorrected and re-sampled to a spatial resolution of 4 m using
222 the AZGCORR software (Azimuth Systems) in conjunction with a 4 m airborne
223 LiDAR DEM. The five geocorrected images were then corrected for limb-
224 brightening, mosaicked and co-registered to the 4 m LiDAR DTM using ENVI
225 4.3 (ITT Visual Information Solutions, Boulder, Colorado) to generate the 4 m
226 ATM imagery comprising Bands 2–10 (Fig. 1c). The reader is referred to Grebby

227 et al. (2011) for further information regarding the processing steps applied to the
228 ATM imagery.

229

230 **Methods**

231 The methodology employed in this study comprises four main steps: a
232 preliminary analysis, followed by lineament enhancement, mapping and analysis
233 and field validation. Each of these steps is discussed in detail below.

234

235 **Preliminary analysis**

236 A preliminary analysis was first undertaken to determine whether the main
237 structural features in the study area could be identified using both the 4 m airborne
238 LiDAR DTM and 4 m ATM imagery. The main structural features found in the
239 Troodos study area are faults and dykes (Figs. 2 and 3). The locations of typical
240 examples of a fault and a dyke were identified and cross-sectional profiles were
241 extracted for these from the airborne LiDAR DTM and ATM imagery for
242 inspection in order to determine the utility of the datasets for mapping the
243 ophiolite structure.

244 The example fault (labelled “A” in Fig. 1b, c) is of a major fault located
245 along a stream transect, which forms a cleft that cuts both sides of a canyon that
246 contains the stream (Fig. 4a). Cross-sectional profiles extracted from the airborne
247 LiDAR DTM and ATM imagery in the locality of this fault are shown in Figs. 4b
248 and 4c, respectively. The fault can be clearly recognised in the LiDAR DTM
249 profile as a decrease in elevation of approximately 0.5 m over a relatively short
250 width of 7 m; forming a linear trough. This fault is also visible in the ATM

251 imagery, albeit as a subtle decrease in brightness (or radiance) with edges defined
252 by relatively abrupt changes in the brightness gradient at both boundaries.

253 The example dyke (labelled “B” in Fig. 1b, c) is located upstream
254 (southwest) of the example fault. The dyke (or possibly a set of dykes) can be
255 seen cutting across the stream to form an upstanding linear ridge feature in Pillow
256 Lavas on the western bank of the stream (Fig. 4d). Cross-sectional profiles
257 extracted from the airborne LiDAR DTM and ATM imagery in the locality of the
258 dyke are shown in Figs. 4e and 4f, respectively. The dyke is clearly recognised as
259 a 3 m wide ridgeline in the LiDAR DTM profile, bounded by abrupt decreases in
260 elevation at both edges. Although the dyke can be identified in the ATM image
261 profile as well, its expression is less conspicuous because of the narrower (~1 m)
262 width of the feature. Nevertheless, the dyke is defined by boundaries caused by
263 abrupt changes in the radiance gradient. Illumination conditions during image
264 acquisition or smoothing effects during processing of the imagery could be
265 responsible for the relatively narrow appearance of this particular dyke in the
266 ATM imagery.

267

268 **Lineament enhancement**

269 It is apparent from the results of the preliminary analysis that both airborne
270 remote sensing datasets are capable of revealing faults and dykes in the uppermost
271 section of the Troodos ophiolite as lineaments. Accordingly, several visual
272 enhancement techniques were applied to the airborne LiDAR DTM and ATM
273 imagery to help generate structural lineament maps for the study area. However,
274 prior to this, Principal Component Analysis (PCA) was first applied to the ATM
275 imagery in order to reduce the number of spectral bands whilst still retaining most

276 of the spectral information contained within the entire dataset. In addition to
277 reducing data dimensionality, the PCA technique is also useful because it
278 enhances spectral information by decorrelating the spectral data in all bands and
279 can be used to segregate noise (Jensen 2005). An examination of the eigenvalues
280 associated with the resulting nine ATM Principal Component (PC) bands revealed
281 that the first three PC bands accounted for 97.5% of the total data variance (Table
282 1). Consequently, the first three PC bands were selected to represent the ATM
283 imagery in further analysis, whereas the six remaining PC bands were discarded.

284

285 *Shaded relief models*

286 Shaded relief models — such as that shown in Fig. 1b — are topographic
287 images that simulate the reflection of artificial light that is incident upon the
288 surface from a user-specified inclination and azimuth. They are generated from
289 DEMs by assigning shades of grey to pixels to represent their reflectance, which
290 is usually calculated from the angle at which light is incident upon the terrain
291 using a Lambertian reflection model (Masoud and Koike 2006). The ability to
292 alter the shading effects by varying the illumination inclination and azimuth
293 angles makes shaded relief models a powerful tool for identifying lineaments in a
294 range of orientations. Here, a series of eight shaded relief models were generated
295 from the airborne LiDAR DTM for azimuth illumination intervals of 45° (e.g., N,
296 NE, E, etc.) and then visually interpreted to produce a lineament map. At each
297 azimuth interval, the illumination inclination angle and the vertical exaggeration
298 of the topographic surface were also systematically varied to try to help reveal as
299 many lineaments as possible.

300

301 *False-colour composite*

302 In order to help identify lineaments using the ATM imagery, a false-colour
303 composite (FCC) image was generated using ENVI 4.3 by assigning the ATM PC
304 Bands 1, 2 and 3 to the red, green and blue channels of the computer monitor,
305 respectively. As a result, subtle variations in the spectral properties of surface
306 materials are typically enhanced in the FCC image through an increase in the
307 colour contrast. Lineaments are then more readily identifiable in the FCC image
308 as linear edges defined by sharp colour differences. A lineament map was
309 therefore produced by visually interpreting the ATM PC FCC.

310

311 *Laplacian filtering*

312 Laplacian filters are a type of convolution filter commonly applied to
313 remote sensing data for lineament mapping applications (Saha et al. 2002; Ali and
314 Pirasteh 2004; Ricchetti and Palombella 2005). These filters are second derivative
315 edge enhancement filters that operate without regard to edge orientation, i.e., they
316 are non-directional. A Laplacian filter was applied to the airborne LiDAR DTM
317 and each of the three ATM PC bands using a 3×3 pixel kernel with a weighting
318 structure such as that shown in Fig. 5. In each case, the filtered image was added
319 back to the original image at a ratio of 9:1 in order to improve the overall image
320 interpretability. Two separate lineament maps were then produced by visually
321 interpreting the filtered LiDAR DTM in addition to a FCC generated from the
322 three filtered ATM PC bands.

323

324 *Morphological transformation*

325 Mathematical morphological operations such as dilation, erosion, opening
326 and closing have also been applied to enhance lineaments in remotely sensed data.
327 One of the most popular morphological techniques for edge detection is the Top
328 Hat transformation (Tripathi et al. 2000; Ricchetti and Palombella 2005). The Top
329 Hat transformation involves closing or opening operations followed by
330 subtraction with the original image:

$$331 \quad \text{Top Hat}(f) = f^B - f \quad (1)$$

$$332 \quad \text{Top Hat}(f) = f - f_B \quad (2)$$

333 where f is the original image, f^B is the image obtained following the closing
334 operation and f_B is the image obtained after the opening operation. The Top Hat
335 transformation which involves the closing operation (that described by Eq. 1) is
336 considered to yield better results for the extraction of structural features such as
337 faults and fractures (Tripathi et al. 2000). Therefore, the closing-based Top Hat
338 transformation was applied to the airborne LiDAR DTM and each of the ATM PC
339 bands using a 3×3 pixel kernel with a weighting of 1 assigned to all elements —
340 a weighting structure such as this avoids introducing directional bias. Again, two
341 separate lineament maps were produced by visually interpreting the Top Hat-
342 transformed LiDAR DTM as well as a FCC generated from the three Top Hat-
343 transformed ATM PC bands.

344

345 **Lineament mapping**

346 A standard approach was adopted in an attempt to maximise both the
347 consistency and objectivity of the visual mapping of lineaments. This involved

348 producing all lineament maps using the ENVI 4.3 software via the following
349 protocol. All enhanced image products were individually displayed in two image
350 windows; one providing a regional perspective (1× zoom) and a second window
351 providing more detailed view (2–4× zoom). Next, each image product was
352 divided into four smaller, equally-sized sections so that each section could be
353 individually examined to help ensure that the entire study area was subjected to a
354 near-uniform visual examination (Parsons and Yearley 1986). Each of these
355 sections was systematically examined for lineaments. Potential lineaments were
356 inspected in order to establish their origin, and those interpreted to be of a
357 geological nature were traced on-screen as line vectors using the overlay tool in
358 the ENVI 4.3 software. The criteria used to determine the length and origin of all
359 lineaments within a single image product and between products was kept constant.
360 Such consistency helps to further reduce the subjectivity of the manual lineament
361 mapping process. Following interpretation, line vectors associated with each
362 image enhancement technique were exported as Shapefiles for subsequent
363 interrogation.

364

365 **Lineament analysis and validation**

366 Lineament maps generated using the above procedure were analysed to
367 evaluate the utility of the airborne LiDAR data and ATM imagery for structural
368 mapping. To do this, the lineament orientations and lengths were extracted from
369 each map by interrogating the Shapefiles in ArcMap (ArcGIS 9.2; ESRI,
370 Redlands, California). Dominant structural trends expressed in the enhanced data
371 products were revealed by plotting the orientation information on rose diagrams
372 using the Stereonet/StereoWin software

373 (<http://www.geo.cornell.edu/geology/faculty/RWA/programs/>). A variety of
374 statistics relating to the numbers and lengths of lineaments were also computed.
375 The spatial distribution of lineaments in the maps were analysed by way of
376 lineament density maps derived using the Spatial Analyst Line Density tool in the
377 ArcMap Toolbox for a search radius of 250 m.

378 A field survey was undertaken to collect structural measurements for the
379 purpose of validating the results of the airborne LiDAR- and ATM-based
380 lineament mapping. The field survey was conducted by measuring the strike and
381 dip of faults and dykes encountered along the transect highlighted in Fig. 1b, c.
382 This transect — which predominantly comprises a stream transect — provides
383 excellent exposure and runs perpendicular to the apparent NW–SE structural trend
384 in the study area. Structural information obtained along this transect and in the
385 adjacent hills should therefore reflect the primary regional structural trends, thus
386 removing the requirement of an extensive study area-wide field survey for
387 validation. During the field survey, only faults extending beyond the local
388 drainage were measured since very minor faults were not anticipated to be
389 detectable in the remotely sensed data products. Field-based structural
390 measurements were plotted on stereonet and rose diagrams (again using
391 Stereonet/StereoWin software) to enable comparison with remote sensing-based
392 lineament data.

393

394 **Results and discussion**

395 **Field-based structural data**

396 Field-based strike and dip measurements of faults and dykes exposed
397 along the 4 km transect enable the most prominent structural trends within the
398 study area to be determined. In the field, individual dykes and less abundant
399 multiple dyke sets were predominantly observed striking NW–SE and dipping
400 steeply towards the NE (Fig. 6a). This is consistent with other observations
401 concerning the attitude of dykes which were made during mapping of the same
402 region (Gass 1960). The average strike orientation for the 64 dykes is computed as
403 318° with relatively little deviation. Nevertheless, minor secondary N–S and E–W
404 trends are apparent. The dip angle was found to vary between 42° and 90° , with
405 an average dip of approximately 70° NE. Conversely, brittle faults do not appear
406 to exhibit a clear dominant trend (Fig. 6b), although the majority of those
407 observed strike between E–W and NW–SE. Dip angles for the field-mapped faults
408 coincide with those of dykes; varying between $40\text{--}90^\circ$ with an average of $\sim 70^\circ$.
409 The dip direction associated with the faults is also variable, with the majority
410 dipping NE. When combined, the field-based structural data for dykes and faults
411 reveals a dominant NW–SE trend within the study area (Fig. 6c). This dominant
412 trend — comprising an average strike of 320° — is primarily dictated by the
413 abundance of NW–SE striking dykes. Minor trends striking E–W and
414 approximately N–S are also apparent in the combined field-based structural data.
415 During fieldwork it became apparent that many of the lineaments previously
416 identified in the remotely sensed data are dykes and not faults. This was a
417 surprising result — we incorrectly expected that dykes would be somewhat less

418 abundant in the uppermost Troodos ophiolitic crust (Basal Group and Pillow Lava
419 sequences) and that major linear structures would be extensional faults. The dykes
420 typically have margin-parallel fractures and are generally upstanding, although in
421 some cases they were observed as eroded-out troughs depending on the rock types
422 they intrude.

423 A major E–W ridge is visible in the remotely sensed data at the western
424 end of the transect and was therefore ground-checked (location C in Fig. 1b, c).
425 This ridge consists of a 285° trending dyke swarm with silicified and sheared
426 dyke margins and parallel fault surfaces (Fig. 3b). Sub-horizontal slickenlines on
427 polished and sheared surfaces indicate a strike-slip history and adjacent brecciated
428 Pillow Lavas indicate intense brittle deformation. This is the most obvious fault
429 zone in the study area. It was assumed to be a dyke prior to field verification
430 because of its positive relief. However, unlike other faults within the study area,
431 this zone is silicified and parallel to a major dyke set and thus erosionally resistant
432 and ridge-forming. Since dykes are not necessarily ridge-forming lineaments and
433 faults are not necessarily erosionally lowered linear troughs, we again emphasise
434 that the follow-on fieldwork was essential for identifying the structural identity of
435 lineaments identified in the remote sensing analysis.

436

437 **Airborne LiDAR- and ATM-based lineament mapping**

438 The six lineament maps and associated rose diagrams produced through
439 the visual interpretation of the enhanced airborne LiDAR DTM and ATM
440 products are shown in Fig. 7. An initial inspection reveals that the dominant NW–
441 SE structural trend observable in the field is also apparent in all six lineament
442 maps. Moreover, the overall spatial coverage of the lineaments is similar for all

443 six maps. The vast majority of lineaments, which most likely correspond to dykes,
444 are confined to the SE sector of the study area with a noticeable lack of lineaments
445 in the NW and the extreme NE corner. The abundance of lineaments in the SE
446 sector is unsurprising because this area is dominated by the Pillow Lava and Basal
447 Group units in which dykes occur. Widespread alluvial–colluvial cover in the NW
448 and Lefkara Formation outcrops in the NE corner explain the lack of lineaments
449 in those areas because these younger cover sediments postdate the magmatic and
450 tectonic events responsible for dyke emplacement and normal faulting.

451 Rose diagrams for all six lineament maps reveal a dominant NW–SE trend
452 for the study area (Fig. 7). This result is corroborated by the field-based structural
453 measurements shown in the Fig. 6c. Several minor secondary trends are also
454 evident in a number of lineament maps; particularly those generated using the Top
455 Hat-transformed LiDAR DTM (Fig. 7c) and Top Hat-transformed ATM PC FCC
456 (Fig. 7d). Of these, the N–S and E–W trends are substantiated by the field
457 measurements. Average lineament orientations are fairly consistent between
458 maps, ranging from approximately 313° for the LiDAR shaded relief model (Fig.
459 7a) to 318° for the Top Hat-transformed LiDAR DTM (Fig. 7c). These average
460 orientations are also comparable to that obtained from the field-based data.
461 Accordingly, it is evident that both the airborne LiDAR and ATM data products
462 are useful tools for revealing the dominant dyke and faulting trends of the
463 Troodos ophiolite.

464 Despite only minor differences in the orientation information for the
465 various enhancement techniques, further interrogation of the lineament maps
466 reveals some notable differences relating to the abundance and lengths of
467 lineaments (Table 2). A maximum number of 316 lineaments were identified
468 using the Laplacian-filtered LiDAR DTM, compared to an average of 213 for the

469 five other enhanced products. With regards to the two data types, the ATM-based
470 enhancement techniques resulted in the identification of 15% more lineaments on
471 average than LiDAR DTM-based techniques, with the exception of the Laplacian-
472 filtered LiDAR DTM. This suggests that lineaments are generally more noticeable
473 in ATM-derived colour composite images than in the greyscale LiDAR DTM
474 products. Nevertheless, the high abundance of lineaments recognised using the
475 Laplacian-filtered DTM could be an indication that this is the most superior
476 technique for enhancing the appearance of lineaments in the airborne LiDAR
477 DTM.

478 Frequency distributions of lineament lengths associated with each
479 enhancement technique are shown in Fig. 8. All distributions appear unimodal and
480 are positively skewed due to a profusion of lineaments with lengths ranging
481 between 50–400 m. The Laplacian-filtered LiDAR DTM is associated with the
482 greatest abundance of short lineaments, and is responsible for both the shortest
483 mapped lineament (38.2 m) and the shortest average lineament length (158.4 m).
484 This, together with the high number of lineaments associated with this
485 enhancement technique, initially suggests that longer lineaments appear
486 segmented in the Laplacian-filtered LiDAR DTM, therefore resulting in shorter
487 but more numerous lineaments. However, evidence of lineament segmentation is
488 not apparent in the Laplacian-filtered LiDAR DTM and the total lineament length
489 is at least 10% longer than for any other technique, indicating that the additional
490 lineaments do not simply arise through the division of lineaments that appear
491 longer in the other enhanced data products.

492 The lineament density maps shown in Fig. 9 reveal the spatial distribution
493 of the lineaments mapped using each of the enhancement techniques. As might be
494 expected due partly to the similarities in the spatial coverage of lineaments in all

495 six maps, the ensuing lineament density maps are also visibly similar. The highest
496 densities are commonly observed in the east of the study area, within the Pillow
497 Lavas (see Fig. 1a). In several maps, smaller regions of high lineament density are
498 also observed towards the NE and slightly due south of the centre, again
499 coinciding with the outcropping of Pillow Lavas. Considering that the field-based
500 data indicates that the vast majority of lineaments in the study area are dykes
501 together with the geological definitions of the Basal Group and Pillow Lava units
502 (e.g., Bear 1960), one would expect the highest lineament densities to be
503 associated with the Basal Group. A likely explanation for why this is not the case
504 could relate to the ability to distinguish lineaments, particularly dykes, from their
505 host different rocks. For example, with regards to the topographic domain, the
506 relative lack of lineaments (in the form of dykes) in the dyke-dominated Basal
507 Group could be due to uniform weathering and erosion of outcrops, which then
508 leads to difficulty in discerning individual or sets of dykes at the surface. On the
509 other hand, the contrast in hardness between dykes and host Pillow Lava rocks
510 appears to result in differential erosion and weathering, thus giving dykes an
511 obvious topographic surface expression. Spectrally, it is also difficult to identify
512 individual dykes in host Basal Group rocks because they effectively comprise the
513 same mineralogical composition. Dykes in the Pillow Lavas, however, are more
514 readily recognisable because of the higher spectral contrast linked to their more
515 disparate mineralogical compositions, grain sizes and jointing characteristics.
516 Likewise, lineaments that correspond to faults are usually easier to trace in the
517 Pillow Lavas than in the Basal Group rocks (Gass 1960).

518 Lineament density maps can also be used to help determine whether
519 lineament maps with greater abundances of lineaments actually contain more
520 information than those with less. If two lineament density maps with considerably

521 different lineament abundances exhibit a strong correlation, then they can
522 essentially be regarded as equivalent, whereas weak correlation suggests that the
523 two maps do indeed contain different information (Parsons and Yearly 1986). The
524 results of the correlation analysis show strong correlations between all lineament
525 density maps (Table 3). Lineament density maps for the Laplacian-filtered ATM
526 PC FCC and Top Hat-transformed LiDAR DTM enhancement techniques are the
527 most weakly correlated, whereas the Laplacian-filtered ATM PC FCC map and
528 the Top Hat-transformed ATM map are the most correlated. Correlation
529 coefficients between the map with the greatest abundance of lineaments (the
530 Laplacian-filtered DTM) and all other maps do not fall below 0.81. This result
531 suggests that all lineament maps essentially contain the same information
532 regardless of the variation in lineament abundance. Also, the results appear to
533 suggest that the additional lineaments identified in the Laplacian-filtered LiDAR
534 DTM are not related to the segmentation of longer lineaments, since higher
535 lineament densities in the affected areas would likely result in somewhat lower
536 correlations than those observed here.

537

538 **Significance of structural trends and implications**

539 Field-based structural measurements collected along the 4 km transect
540 through the study area show that dykes primarily dip to the NE. This finding is in
541 agreement with the placement of the study area on the western flank of the
542 Larnaca graben proposed by Varga and Moores (1985). The prevailing NW–SE
543 trend revealed by field-based structural measurements is consistent with that
544 expected for an extensional setting. Although dykes appear to dictate this trend, an
545 additional contribution also originates from normal faulting during graben

546 development and dyke injection (Gass 1960). Whilst there is a slight indication of
547 dyke-parallel faulting in the field-based data, the rather variable orientations of the
548 faults recorded along the transect most likely reflect local deformation and
549 possibly younger faulting subsequent to initial formation of the ophiolitic crust.
550 The secondary N-S trend apparent in the field-based data is consistent with a later
551 stage of faulting previously reported in the vicinity of the study area (Gass 1960;
552 Boyle and Robertson 1984).

553 The main NW–SE and N-S structural trends observed in the study area are
554 also reciprocated in lineament maps generated using the enhanced airborne
555 LiDAR and ATM products. Moreover, these lineament maps are able to resolve
556 structural information in much greater spatial detail than the existing geological
557 maps of the study area. These findings are important because they demonstrate
558 that high-resolution remotely sensed datasets can be used to complement field-
559 based structural mapping. Specifically, when used in conjunction with field-based
560 mapping, airborne datasets clearly offer the potential to help make detailed and
561 comprehensive structural mapping a more time- and cost-efficient process.

562 Obtained using a combined remote sensing–fieldwork structural mapping
563 approach, our results reveal that there is a fundamental NW-trending steep
564 structural grain wherever the ophiolitic rocks crop out. Based on this, it is also
565 likely that this structural grain exists in surrounding areas under the Lefkara
566 Formation and alluvial–colluvial cover. This fundamental structural grain was
567 found to be dominated by parallel individual dykes and dyke swarms and less
568 abundant normal faults. Otherwise, the hummocky Pillow Lava terrain is
569 characterised by diverse erupted sequences that are complexly stacked and
570 overlapping without other major cross-cutting tectonic structures (Fig. 3a). The
571 NW–SE structural fabric identified in the Pillow Lava and Basal Group rocks and

572 interpreted to occur under sedimentary cover elsewhere in the study area, may be
573 an important consideration for future resource exploration efforts. This is because
574 deep and steep faults and fractured dyke margins may host groundwater, and
575 because major normal faults may have originally been hydrothermal fluid
576 pathways and therefore potential sites of massive sulphide (copper) mineralisation
577 (Fig. 3c, d). Another major implication of this study is that the methods presented
578 can be readily utilised to map dyke and fault trends in greater detail across the
579 ophiolite. Ultimately, this may help to better elucidate the spreading structure of
580 the Troodos ophiolite.

581

582 **Conclusions**

583 This study investigates the efficacy of high-resolution airborne LiDAR
584 topographic data and ATM imagery for assisting detailed structural mapping of
585 the vegetated ophiolitic rocks and sedimentary cover in an upper section of the
586 Troodos ophiolite. To the best of our knowledge, this is the first attempt to apply
587 airborne LiDAR to detailed structural mapping of ophiolitic rocks. Despite
588 widespread vegetation cover, a preliminary analysis showed that the main
589 structural features — dykes and faults — were recognisable in both the 4 m
590 airborne LiDAR-derived DTM and 4 m ATM imagery as lineaments defined by
591 edges. Accordingly, several different edge enhancement techniques were applied
592 to the datasets in an attempt to augment the visual identification and mapping of
593 lineaments. The resulting lineament maps present structural information in much
594 greater spatial detail than the existing geological maps of the study area.
595 Moreover, the predominant strike trends of lineaments in all maps were found to
596 be consistent with field-based structural data acquired along a transect, in addition

597 to other observations made by ourselves and other workers in the vicinity. The
598 dominant trend in the study area is orientated NW–SE and corresponds at first-
599 order to the direction of dykes injections and extensional faulting associated with
600 the spreading axis of the proposed palaeo-Larnaca graben system. Overall, the
601 results of this study demonstrate the significant potential to produce detailed and
602 comprehensive structural maps efficiently, by using airborne LiDAR data or
603 airborne spectral imagery in conjunction with field-based mapping.

604 Whilst the results of this study have direct relevance to structural mapping
605 of the Troodos ophiolite and other ophiolites, it is anticipated that high-resolution
606 airborne LiDAR data and airborne spectral imagery can be readily used to
607 augment detailed structural mapping in other settings with a similar
608 Mediterranean climate and vegetation cover. In fact, with the capability of
609 acquiring high-resolution topographic data in densely forested terrain, airborne
610 LiDAR clearly has the potential to be a valuable tool for many aspects of
611 structural mapping in any geological setting, irrespective of vegetation cover.
612 However, the efficacy of airborne LiDAR will be dependent on the generation of
613 an adequate DTM. In densely forested terrain this may require a high LiDAR
614 point density to help maximise the number of ground returns. Conversely,
615 airborne spectral imagery is likely to be of limited use in areas where structural
616 features are subtly expressed in the terrain beneath tall dense vegetation cover.

617 Although accurate and detailed structural mapping using a manual
618 approach was not time-consuming in this case, automated lineament extraction
619 algorithms would be more efficient for larger map areas. In this respect, further
620 research is required to help improve differentiation between lineaments of a
621 geological origin and lineaments of non-geological significance. An integrated
622 spectral–topographic approach which combines diagnostic morphometric and

623 spectral characteristics could offer additional discriminatory power to help reduce
624 this confusion.

625

626

627

628

629

630

631 **Acknowledgements** This work was primarily supported through a Natural Environment
632 Research Council (NERC) CASE Studentship (NE/F00673X/1) in collaboration with the British
633 Geological Survey (BGS) University Funding Initiative, awarded to SG. We gratefully
634 acknowledge the NERC Airborne Research and Survey Facility (grant MC04/30) for data
635 acquisition and the Unit for Landscape Modelling for data pre-processing. We would also like to
636 express our gratitude to the Geological Survey Department of Cyprus (GSD) for providing the
637 digital geological maps, to Dr. Stelios Nicolaides (GSD) and Dr. Simon Jowitt (Monash
638 University) for invaluable logistical and scientific help in the field, and to Luke Bateson (BGS)
639 and Professor Danny Donoghue (Durham University) for AZGCORR and TerraScan software
640 support, respectively. Professor Richard Allmendinger (Cornell University) is also thanked for
641 providing free access to the Stereonet/StereoWin software. SG is grateful to the Geological
642 Remote Sensing Group for receipt of a Student Fieldwork and Travel Award. JN publishes with
643 permission of the Executive Director, British Geological Survey (NERC). We thank Dr. Terry
644 Pavlis and an anonymous reviewer for their comments and suggestions which helped to improve
645 the quality of this manuscript.

646

647

648

649

650

651 **References**

- 652 Ali SA, Pirasteh S (2004) Geological applications of Landsat Enhanced Thematic Mapper (ETM)
653 data and Geographic Information System (GIS): mapping and structural interpretation in south-
654 west Iran, Zagros Structural Belt. *Int J Remote Sens* 25:4715–4727
655
- 656 Argialas DP, Mavrantza OD (2004) Comparison of edge detection and Hough transform
657 techniques for the extraction of geologic features. *Int Arch Photogramm Remote Sens Spat Inf Sci*
658 34:790–795
659
- 660 Arrowsmith JR, Zielke O (2009) Tectonic geomorphology of the San Andreas Fault zone from
661 high resolution topography: An example from the Cholame segment. *Geomorphology* 113:70–81
662
- 663 Axelsson P (2000) DEM Generation from Laser Scanner Data Using Adaptive TIN Models. *Int*
664 *Arch Photogramm Remote Sens* 33:110–117
665
- 666 Barnes JW, Lisle RJ (2004) *Basic Geological Mapping*, Fourth edition. John Wiley and Sons,
667 Chichester
668
- 669 Bear LM (1960) The geology and mineral resources of the Akaki-Lythrodondha area, Memoir 3.
670 Geological Survey Department, Cyprus
671
- 672 Boyle JF, Robertson AHF (1984) Evolving metallogenesis at the Troodos spreading axis. *Geol*
673 *Soc Lon Spec Publ* 13:169–181
674
- 675 Corgne S, Magagi R, Yergeau M, Sylla D (2010) An integrated approach to hydro-geological
676 lineament mapping of a semi-arid region of West Africa using Radarsat-1 and GIS. *Remote Sens*
677 *Environ* 114:1863–1875
678
- 679 Cunningham D, Grebby S, Tansey K, Gosar A, Kastelic V (2006) Application of airborne LiDAR
680 to mapping seismogenic faults in forested mountainous terrain, southeastern Alps, Slovenia.
681 *Geophys Res Lett* 33:L20308
682
- 683 Fitton NC, Cox SJD (1998) Optimising the application of the Hough transform for automatic
684 feature extraction from geoscientific images. *Comput Geosci* 24:933–951
685
- 686 Gass IG (1960) The geology and mineral resources of the Dhali area, Memoir 4. Geological
687 Survey Department, Cyprus
688
- 689 Gass IG (1968) Is the Troodos massif of Cyprus a fragment of Mesozoic ocean crust? *Nature*
690 220:39–42
691

692 Grebby S, Cunningham D, Naden J, Tansey K (2010) Lithological mapping of the Troodos
693 ophiolite, Cyprus, using airborne LiDAR topographic data. *Remote Sens Environ* 114:713–724
694
695 Grebby S, Naden J, Cunningham D, Tansey K (2011) Integrating airborne multispectral imagery
696 and airborne LiDAR data for enhanced lithological mapping in vegetated terrain. *Remote Sens*
697 *Environ* 115:214–226
698
699 Harding DJ, Berghoff GS (2000) Fault scarp detection beneath dense vegetation cover: airborne
700 lidar mapping of the Seattle fault zone, Bainbridge Island, Washington State. In: *Proceedings of*
701 *the American Society of Photogrammetry and Remote Sensing Annual Conference*, Washington
702 D.C., May 2000. American Society of Photogrammetry and Remote Sensing, Bethesda, Maryland
703
704 Haugerud RA, Harding DJ, Johnson SY, Harless JL, Weaver CS, Sherrod BL (2003) High-
705 resolution Lidar topography of the Puget Lowland, Washington — A bonanza for earth science.
706 *GSA Today* 13:4–10
707
708 Hill RA, Wilson AK, George M, Hinsley SA (2010) Mapping tree species in temperate deciduous
709 woodland using time-series multi-spectral data. *Appl Veg Sci* 13:86–99
710
711 Jensen JR (2005) *Introductory digital image processing: a remote sensing perspective*. Prentice
712 Hall, New Jersey
713
714 Jordan G, Schott B (2005) Application of wavelet analysis to the study of spatial pattern of
715 morphotectonic lineaments in digital terrain models. A case study. *Remote Sens Environ* 94:31–38
716
717 Karnieli A, Meisels A, Fisher L, Arkin Y (1996) Automatic extraction and evaluation of
718 geological linear features from digital remote sensing data using a Hough transform. *Photogramm*
719 *Eng Remote Sens* 62:525–531
720
721 Koike K, Nagano S, Kawaba K (1998) Construction and analysis of interpreted fracture planes
722 through combination of satellite-image derived lineaments and digital elevation model data.
723 *Comput Geosci* 24:573–583
724
725 Koike K, Nagano S, Ohmi M (1995) Lineament analysis of satellite images using a Segment
726 Tracing Algorithm (STA). *Comput Geosci* 21:1091–1104
727
728 Kraus K, Pfeifer N (1998) Determination of terrain models in wooded areas with airborne laser
729 scanner data. *ISPRS J Photogramm Remote Sens* 53:193–203
730
731 Kresic N (1995) Remote sensing of tectonic fabric controlling groundwater flow in Dinaric Karst.
732 *Remote Sens Environ* 53:85–90

733

734 Masoud A, Koike K (2006) Tectonic architecture through Landsat-7 ETM+/SRTM DEM-derived
735 lineaments and relationship to the hydrogeologic setting in Siwa region, NW Egypt. *J Afr Earth*
736 *Sci* 45:467–477

737

738 Moore GK, Waltz FA (1983) Objective procedures for lineament enhancement and extraction.
739 *Photogramm Eng Remote Sens* 49:641–647

740

741 Moores EM, Vine FJ (1971) Troodos Massif, Cyprus and other ophiolites as oceanic crust:
742 evaluation and implications. *Philos T Roy Soc A* 268:443–467

743

744 Mountrakis D, Pavlides S, Zouros N, Astaras T, Chatzipetros A (1998) Seismic fault geometry and
745 kinematics of the 13 May 1995 Western Macedonia (Greece) earthquake. *J Geodyn* 26:175–196

746

747 Nyborg M, Berglund, J., Triumf C-A (2007) Detection of lineaments using airborne laser scanning
748 technology: Laxemar-Simpevarp, Sweden. *Hydrogeol J* 15:29–32

749

750 O'Leary DW, Friedman JD, Pohn HA (1976) Lineament, linear, lineation - some proposed new
751 standards for old terms. *Geol Soc Am Bull* 87:1463–1469

752

753 Parsons AJ, Yearley, R J (1986) An analysis of geologic lineaments seen on LANDSAT MSS
754 imagery. *Int J Remote Sens* 7:1773–1782

755

756 Pavlis TL, Bruhn RL (2011) Application of LIDAR to resolving bedrock structure in areas of poor
757 exposure: An example from the STEEP study area, southern Alaska. *Geol Soc Am Bull* 123:206–
758 217

759

760 Peña SA, Abdelsalam MG (2006) Orbital remote sensing for geological mapping in southern
761 Tunisia: Implication for oil and gas exploration. *J Afr Earth Sci* 44:203-219

762

763 Prentice CS, Crosby CJ, Harding DJ, Haugerud RA, Merritts DJ, Gardner TW, Koehler RD,
764 Baldwin JN (2003) Northern California LIDAR data: A tool for mapping the San Andreas Fault
765 and pleistocene marine terraces in heavily vegetated terrain. Paper presented at American
766 Geophysical Union Fall Meeting, San Francisco, California, December 2003

767

768 Qari MYHT (1991) Application of Landsat TM data to geological studies, Al-Khabt Area,
769 Southern Arabian Shield. *Photogramm Eng Remote Sens* 57:421–429

770

771 Ricchetti E, Palombella, M (2005) Application of Landsat 7 ETM+ imagery for geological
772 lineament analysis of Southern Italy. In: *Proceedings of IGARSS 2005, Geoscience and Remote*
773 *Sensing Symposium, Seoul, South Korea, July 2005. IEEE International*

774
775 Saha AK, Gupta, RP, Arora MK (2002) GIS-based landslide hazard zonation in the Bhagirathi
776 (Ganga) Valley, Himalayas. *Int J Remote Sens* 23:357–369
777
778 Süzen ML, Toprak V (1998) Filtering of satellite images in geological lineament analyses: an
779 application to a fault zone in Central Turkey. *Int J Remote Sens* 19:1101–1114
780
781 Tripathi NK, Gokhale KVGK, Siddiqui MU (2000) Directional morphological image transforms
782 for lineament extraction from remotely sensed images. *Int J Remote Sens* 21:3281–3292
783
784 Varga RJ, Moores EM (1985) Spreading structure of the Troodos ophiolite, Cyprus. *Geology*
785 13:846–850
786
787 Wallace J, Morris B, Howarth P (2006) Identifying structural trend with fractal dimension and
788 topography. *Geology* 34:901–904
789
790 Wladis D (1999) Automatic lineament detection using digital elevation models with second
791 derivative filters. *Photogramm Eng Remote Sens* 65:453–458
792
793
794
795
796
797
798
799
800
801
802
803
804
805
806
807
808

809 **Figure captions**

810 **Fig. 1. a** Location and geology (at 1:31,680- and 1:250,000-scale) of the Troodos ophiolite and the
811 study area. **b** Shaded relief model of the study area generated from the 4 m airborne LiDAR DTM.
812 **c** A red-green-blue true-colour composite image of the study area generating using bands 5, 3, and
813 2 of the 4 m ATM imagery. Labels A, B and C in **b** and **c** indicate the locations of the example
814 fault, dyke and fault ridge shown in Fig. 4a, d and Fig. 3b, respectively. Red shading in **b** and **c**
815 depicts transect along which field-based structural data were acquired. Digital geology provided by
816 the Cyprus Geological Survey Department.

817

818 **Fig. 2.** Field photographs showing typical examples of structural features observed in the study
819 area. **a** Set of NW-SE striking dykes intruding Pillow Lavas; **b** and **c** brittle fault zones in Pillow
820 Lavas; **d** NW-SE trending dykes expressed in the landscape; **e** and **f** upstanding dykes intruding
821 Pillow Lavas.

822

823 **Fig. 3.** Important geological features of the study area. **a** Typical hummocky Pillow Lava
824 landscape comprising stacks of erupted lavas devoid of steep structures; **b** upstanding silicified
825 strike-slip fault zone which was assumed to be a dyke prior to field verification (location C in Fig.
826 1b); **c** parallel dyke swarm with abundant dyke margin-parallel fractures; **d** gossan alteration
827 within Pillow Lavas and along dyke margins and joints.

828

829 **Fig. 4.** Expression of the main types of structural features in the remotely sensed data. **a** Field
830 photograph of the example fault at location A in Fig. 1b, c, and cross-sectional profiles showing
831 the expression of this fault cleft as a trough in **b** the airborne LiDAR DTM and **c** ATM Band 2
832 image. **d** Field photograph of the example dyke(s) at location B in Fig. 1b, c, and cross-sectional
833 profiles showing the expression of the dyke(s) as a ridge in **e** the airborne LiDAR DTM and **f**
834 ATM Band 5 image.

835

836 **Fig. 5.** Weighting structure of the 3×3 pixel kernel used in Laplacian filtering.

837

838 **Fig. 6.** Structural data obtained through field-based mapping along the transect indicated in Fig.
839 1b, c. **a** Equal-area stereonet plot revealing a dominant NW-SE trend and steep NE dip for 64
840 dykes observed in the field. **b** Equal-area stereonet plot showing the variable strike and dip for 16
841 faults mapped in the field. **c** Equal-area stereonet contour plot of poles to planes for the combined
842 dyke and fault data (shown in **a** and **b**, respectively) reveals a dominant NW-SE structural trend
843 within the study area.

844

845 **Fig. 7.** Lineament maps and rose diagrams (inset) generated through visual interpretation of **a**
846 LiDAR shaded relief model (15%), **b** ATM PC FCC (17%), **c** Top Hat-transformed LiDAR DTM
847 (12%), **d** Top Hat-transformed ATM PC FCC (12%), **e** Laplacian-filtered LiDAR DTM (16%) and
848 **f** Laplacian-filtered ATM PC FCC (16%). Bracketed percentages denote proportion of lineaments
849 represented by outer circle in corresponding rose diagrams (see Table 2 for total number of
850 lineaments in each map). Average orientations are indicated on rose diagrams.

851

852 **Fig. 8.** Frequency distributions of lineament lengths mapped using the various enhanced data
853 products. **a** LiDAR shaded relief model; **b** ATM PC FCC; **c** Top Hat-transformed LiDAR DTM; **d**
854 Top Hat-transformed ATM PC FCC; **e** Laplacian-filtered LiDAR DTM; **f** Laplacian-filtered ATM
855 PC FCC.

856

857 **Fig. 9.** Lineament density maps derived from lineament maps generated through visual
858 interpretation of **a** LiDAR shaded relief model, **b** ATM PC FCC, **c** Top Hat-transformed LiDAR
859 DTM, **d** Top Hat-transformed ATM PC FCC, **e** Laplacian-filtered LiDAR DTM and **f** Laplacian-
860 filtered ATM PC FCC. Shading represents low (white) to high (black) lineament density.

861

862

863

864

865

866

867

868

869

870

871

872

873

874

875

876

877

878

879

880 **Table 1.** Eigenvalues and eigenvector loadings for the first three PC bands derived from the
 881 application of PCA to ATM Bands 2–10.

Eigenvectors	PC1	PC2	PC3
ATM 2	0.33	-0.40	-0.19
ATM 3	0.35	-0.32	-0.20
ATM 4	0.35	-0.26	-0.16
ATM 5	0.36	-0.17	-0.14
ATM 6	0.36	0.19	-0.19
ATM 7	0.33	0.47	-0.19
ATM 8	0.30	0.57	-0.05
ATM 9	0.32	0.17	0.50
ATM 10	0.29	-0.19	0.74
Eigenvalues	7.25	1.00	0.53
Variance (%)	80.56	11.10	5.84
Cumulative variance (%)	80.56	91.66	97.50

882

883

884

885 **Table 2.** Statistics relating to the abundance and lengths of lineaments identified using the various
 886 enhancement techniques.

Enhancement technique	Number of lineaments	Min. length (m)	Max. length (m)	Average length (m)	Total length (m)
LiDAR shaded relief model	192	51.1	801.0	207.4	39,817.5
ATM PC FCC	227	38.2	714.7	167.5	38,021.0
Top Hat-transformed LiDAR DTM	199	55.2	709.2	199.5	39,707.1
Top Hat-transformed ATM PC FCC	210	52.5	665.4	217.0	45,563.1
Laplacian-filtered LiDAR DTM	316	37.7	735.1	158.4	50,059.3
Laplacian-filtered ATM PC FCC	239	53.5	868.3	174.9	41,791.4

887

888

889

890

891

892 **Table 3.** Correlation matrix for the lineament density maps.

	LiDAR shaded relief model	ATM PC FCC	Top Hat-transformed LiDAR DTM	Top Hat-transformed ATM PC FCC	Laplacian-filtered LiDAR DTM	Laplacian-filtered ATM PC FCC
LiDAR shaded relief model	–					
ATM PC FCC	0.82	–				
Top Hat-transformed LiDAR DTM	0.89	0.79	–			
Top Hat-transformed ATM PC FCC	0.87	0.87	0.83	–		
Laplacian-filtered LiDAR DTM	0.88	0.81	0.84	0.85	–	
Laplacian-filtered ATM PC FCC	0.81	0.87	0.76	0.90	0.81	–

893

894

895

896

897

898

899

900

901

902

903

904

905

906

907

908

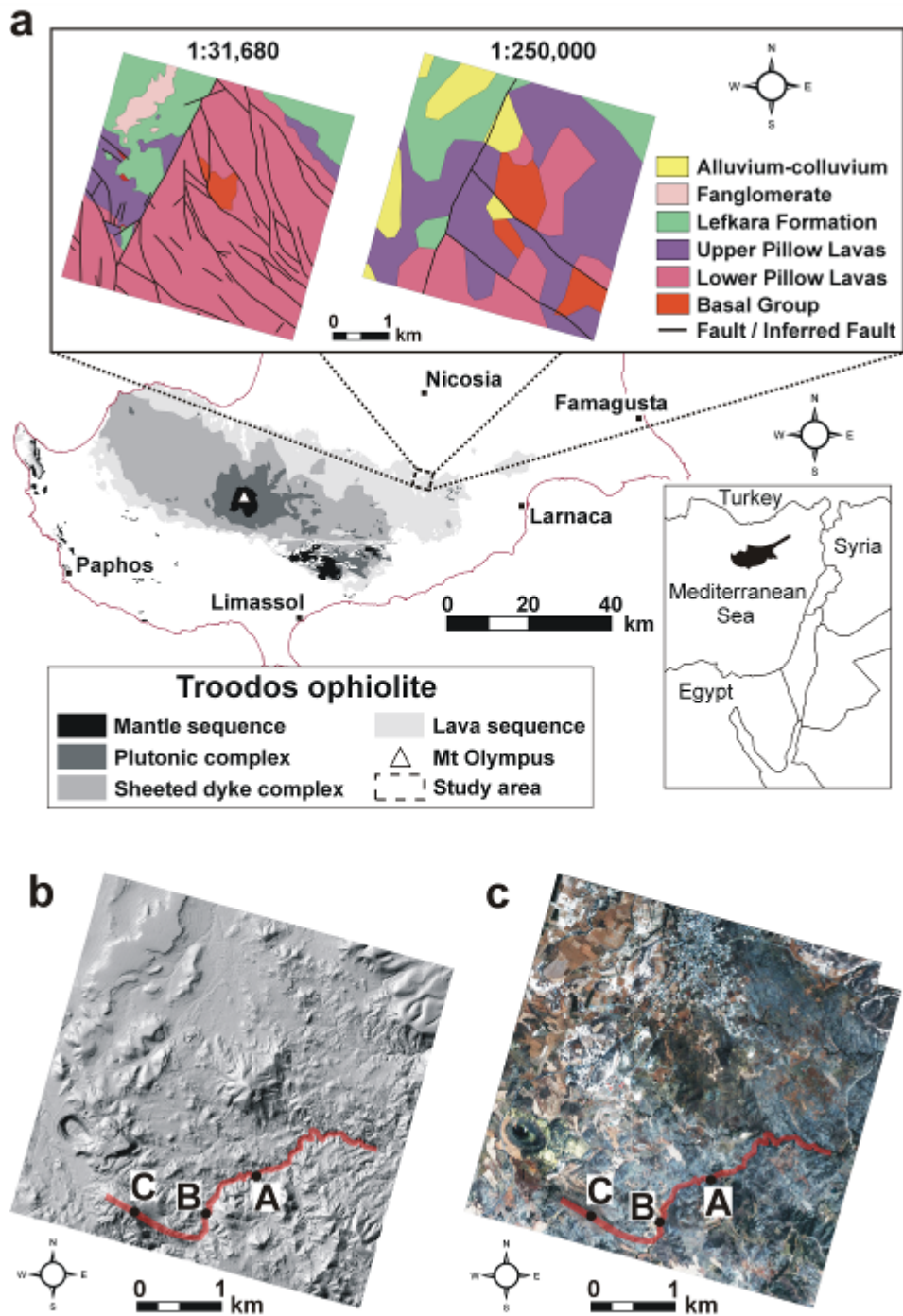
909

910

911

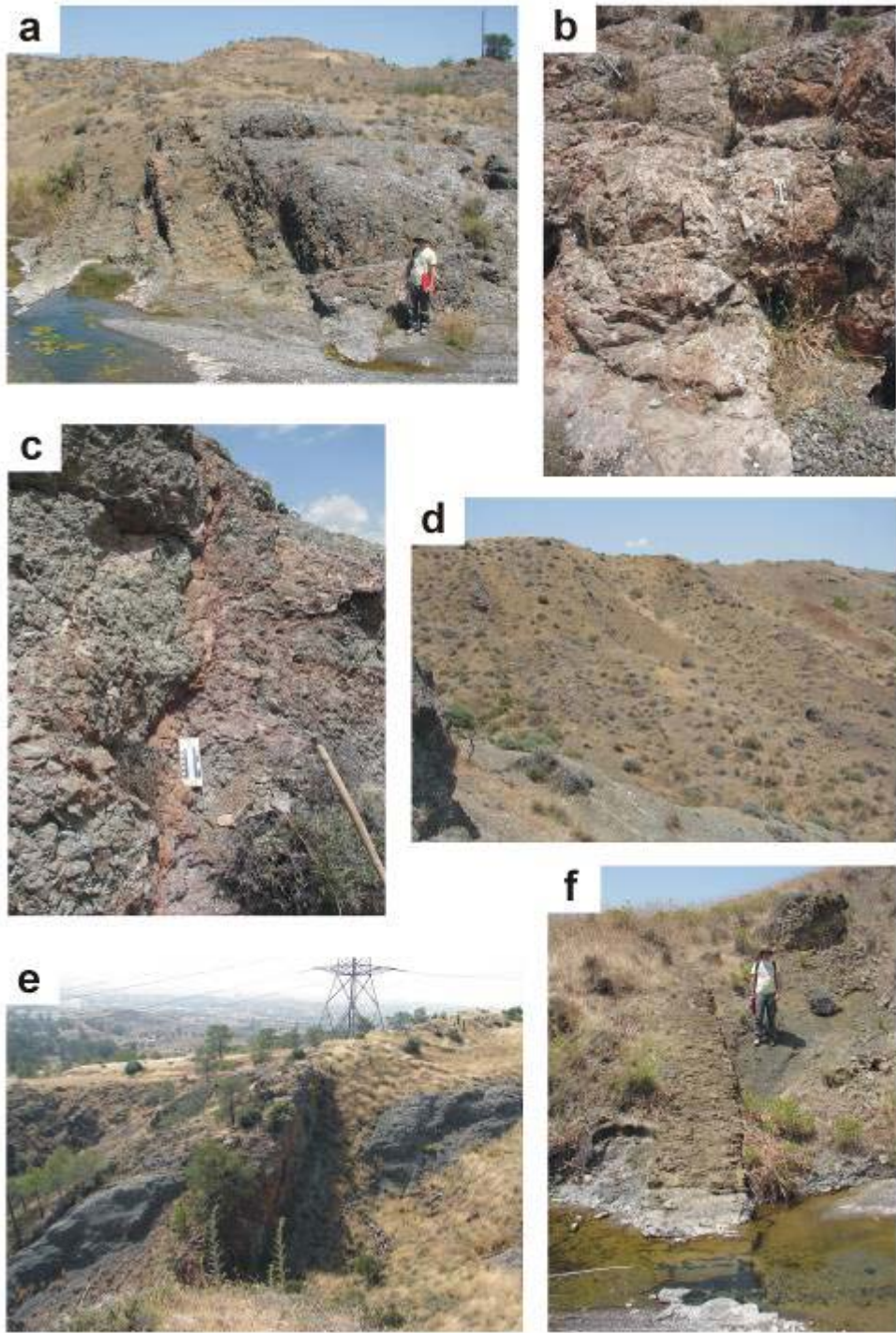
912

913



914
915
916
917

FIG.1



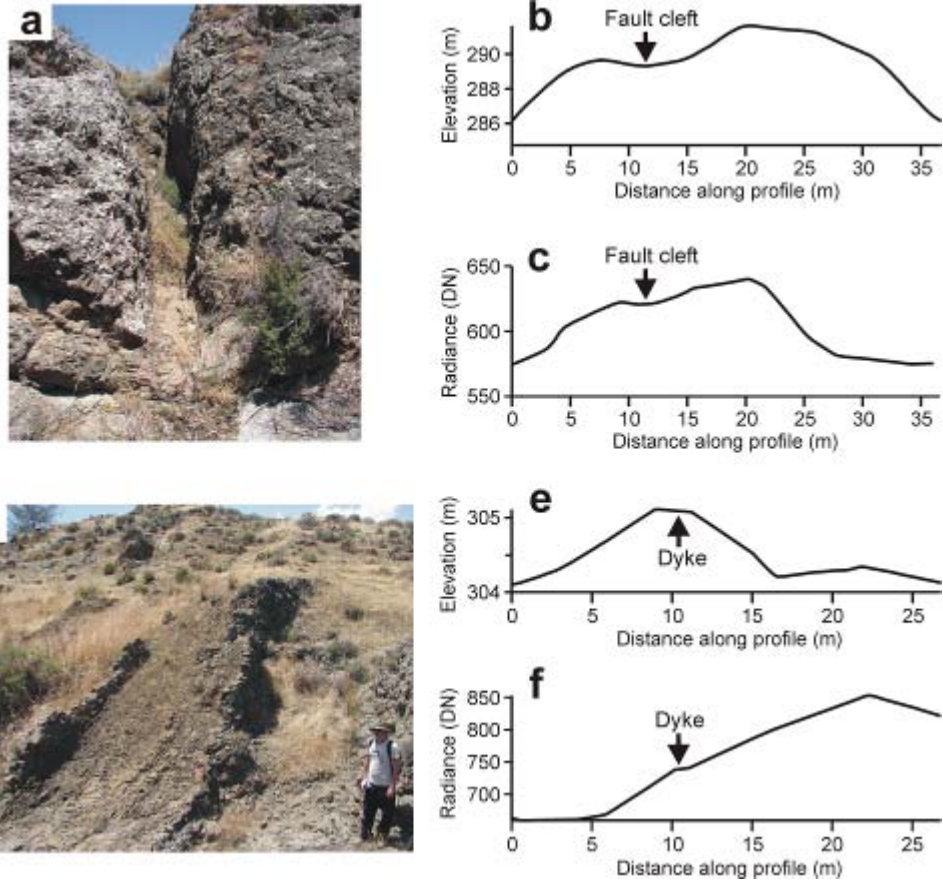
918
919
920
921
922
923
924
925

Fig.2



926
 927
 928
 929
 930
 931
 932
 933
 934
 935

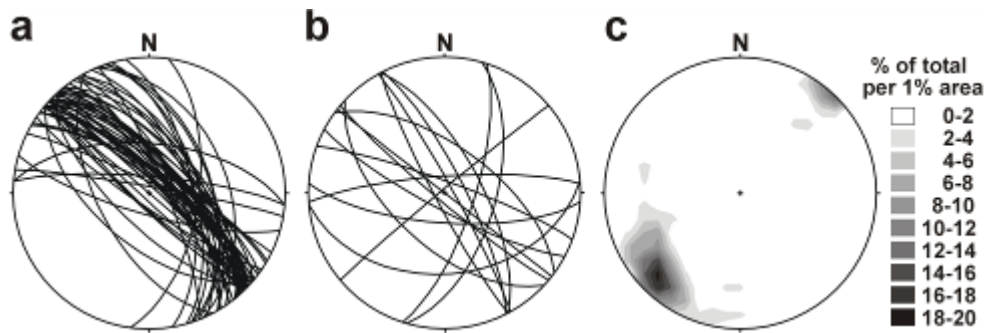
Fig. 3



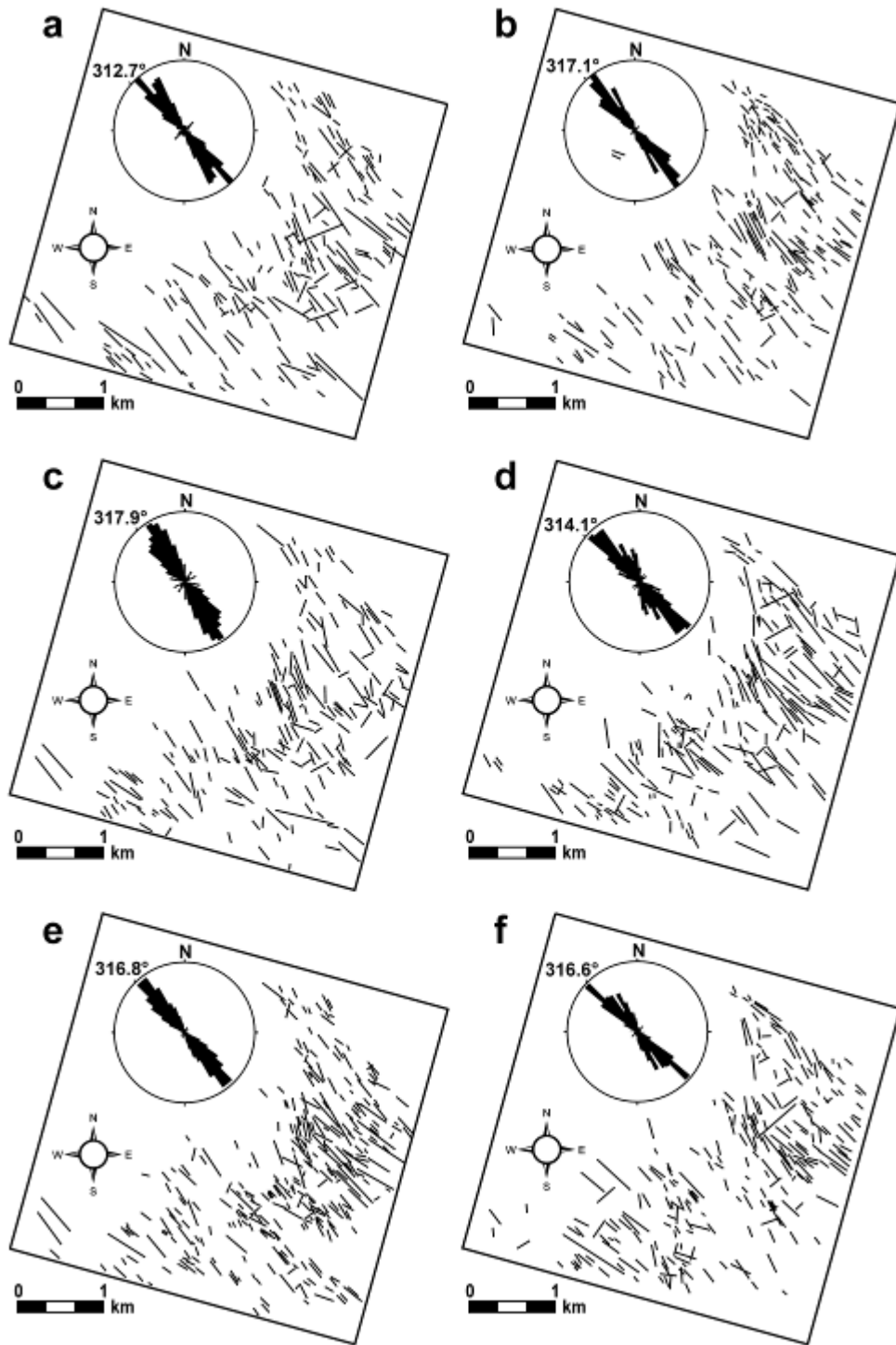
936
937 **Fig. 4**
938
939
940

0	-1	0
-1	4	-1
0	-1	0

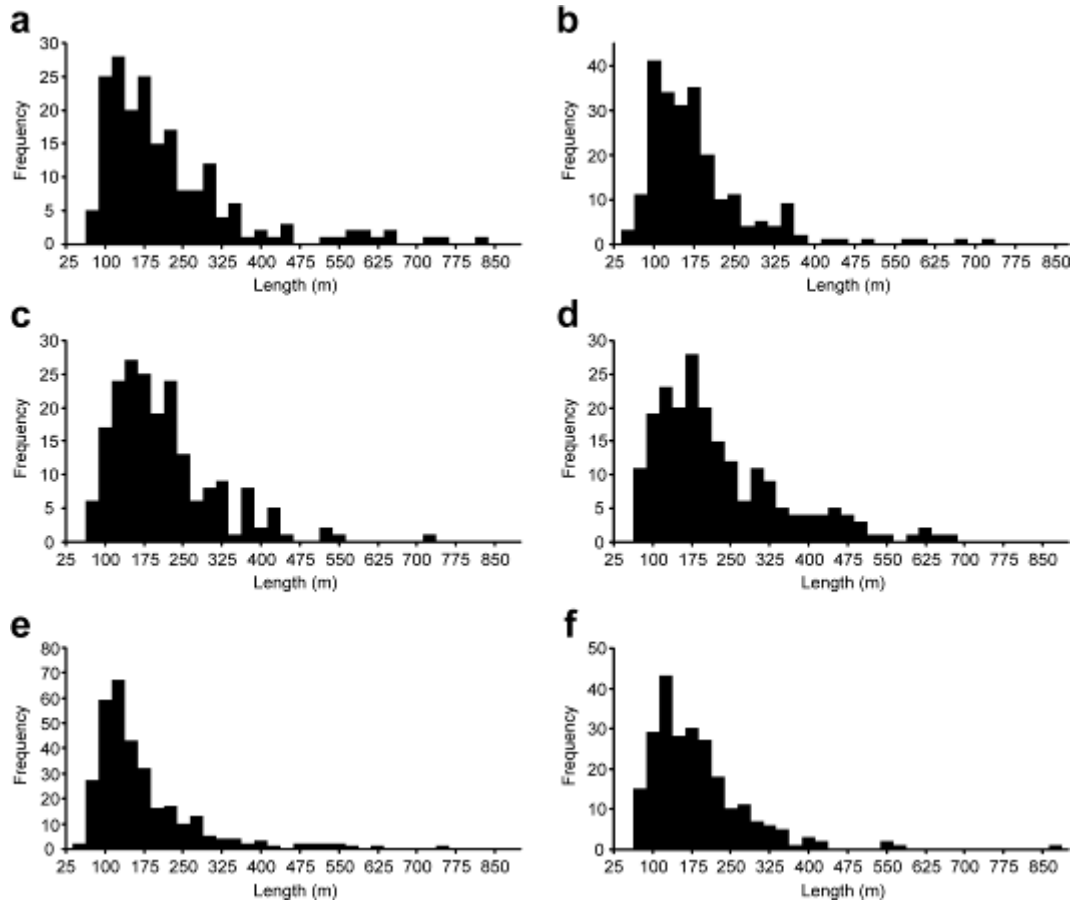
941
942 **Fig. 5**
943
944
945



946
947 **Fig. 6**
948

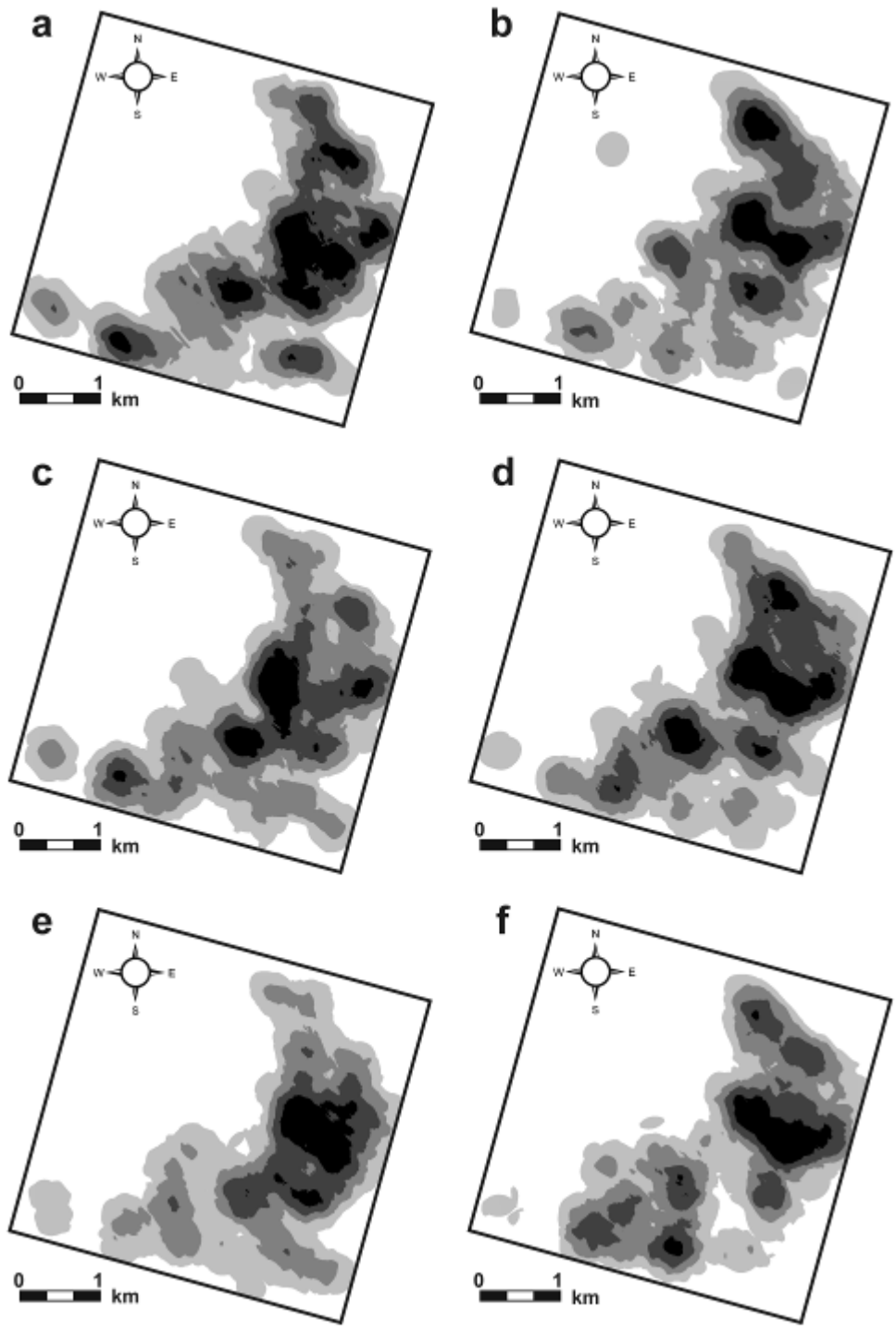


949
 950 **Fig.7**
 951
 952



953
 954
 955
 956

Fig. 8



957
958 **Fig. 9**